Comput Mech
DOI 10.1007/s00466-009-0365-8

ORIGINAL PAPER

Torsional rigidity of a circular bar with multiple circular inclusions using the null-field integral approach

Jeng-Tzong Chen · Ying-Te Lee

Received: 27 October 2008 / Accepted: 10 January 2009

Abstract In this article, a systematic approach is proposed to calculate the torsional rigidity and stress of a circular bar containing multiple circular inclusions. To fully capture the circular geometries, the kernel function is expanded to the degenerate form and the boundary density is expressed into Fourier series. The approach is seen as a semi-analytical manner since error purely attributes to the truncation of Fourier series. By collocating the null-field point exactly on the real boundary and matching the boundary condition, a linear algebraic system is obtained. Convergence study shows that only a few number of Fourier series terms can yield acceptable results. Finally, torsion problems are revisited to check the validity of our method. Not only the torsional rigidities but also the stresses of multiple inclusions are also obtained by using the present approach.

Keywords Torsional rigidity · Null-field integral equation · Degenerate kernel · Fourier series · Inclusion

1 Introduction

In the past, multiply-connected Laplace problems have been solved either by conformal mapping or by other techniques. Ling [14] solved the torsion problem of a circular bar with several holes. Muskhelishvili [19] solved the problem of a circular bar reinforced by an eccentric circular inclusion. Chen and Weng [8] have introduced conformal mapping with a Laurent series expansion to analyze the Saint-Venant torsion problem. They concerned with an eccentric bar of different materials with an imperfect interface under torque. Since the conformal mapping is limited to the doubly-connected region, it encounters difficulty for multiple inclusions. Therefore, many researchers have paid more attentions on other techniques or numerical methods. In 1983, Caulk [3] developed a special boundary integral method to deal with the problem of a torsion bar with circular holes. Katsikadelis and Sapountzakis [11] used the boundary element method to solve the problem of an elliptic bar including one and two elliptic inclusions. Also, a practical problem of a rectangular concrete containing a Steel-I beam was concerned in their research. Later, Sapountzakis and Mokos [22–24] extended to deal with the nonuniform torsion problem that the composite bar is subject to an arbitrarily concentrated or distributed twisting moment. Shams-Ahmadi and Chou [25] used the complex variable boundary element method (CVBEM) to solve the torsion problem of composite shafts with arbitrary number of inclusions of different materials. Ang and Kang [1] developed a general formulation for solving the second-order elliptic partial differential equation for a multiply-connected region in a different version of CVBEM. Petrov [21] developed an effective technique of boundary element method (BEM) to determine torsion, shear and other characteristics of beam cross-sections of arbitrary complex shape including multiply-connected cross sections. Tang [27] utilized the singular and hypersingular formulations to solve the torsion problem with inclusions and/or cracks.

Recently, meshless methods [10,26] become very popular, since it is free of mesh generation and only nodes are needed. The present formulation can be seen as one kind of

J.-T. Chen (✉) · Y.-T. Lee
Department of Harbor and River Engineering,
National Taiwan Ocean University,
Keelung 20224, Taiwan
e-mail: jtchen@mail.ntou.edu.tw

J.-T. Chen
Department of Mechanical and Mechatronics Engineering,
National Taiwan Ocean University,
Keelung 20224, Taiwan

Published online: 10 February 2009

meshless methods, since only the collocation points on the real boundary are required to satisfy the boundary condition. Mogilevskaya and Crouch [16] have solved the problem of an infinite plane containing arbitrary number of circular inclusions based on the complex-variable singular integral equation. Later, they [9] utilized Somigliana's formula and Fourier series for elasticity problems with circular boundaries. In their analysis procedure, the authors used the Fourier series to simulate the boundary densities on the circular geometry. Besides, they used the complex variable and the residue theorem to calculate the singular integrals. Therefore, for calculating an integral over a circular boundary, they didn't expand the fundamental solution to degenerate kernel by using the polar coordinates of local system. By moving the null-field point exactly on the real boundary, the boundary integral can be easily determined using series sums in our formulation due to the introduction of degenerate kernels. Also, it is free of worrying how to choose the collocation points, since uniform collocation along the circular boundary yields a well-conditioned matrix. Caulk [3] proposed a special BIEM to determine the torsional rigidity of a circular bar with circular holes. He pointed out that Ling's result of three holes deviated from his data. Chen et al. [7] supported the Caulk's comment by using the null-field integral approach. On the other hand, Bird and Steele [2] found the discrepancy between the Naghdi's solution [20] and their data for the beam bending problem with four holes. Also, Chen et al.'s result [4] agreed with the Naghdi's result. Following the success of [7], we extend to solve torsion problems with multiple circular inclusions. It is noted that we can deal with other shape of cross section in our approach, if the degenerate kernels corresponding to the special geometry are available. For example, degenerate kernel for the ellipse can be found in the book of Morse and Feshbach [17]. It is straightforward to extend the present method to solve the problem with the geometry of an ellipse. Unfortunately, some formulae are not found in the mathematical handbook or were not derived by mathematicians for special geometry. That is to say, it is a challenging work in deriving the degenerate kernel for a special geometry case.

In this paper, the null-field integral equation is utilized to solve the Saint-Venant torsion problem of a circular bar with circular inclusions. The mathematical tools, the degenerate kernel for the fundamental solution and Fourier series for the boundary density, are utilized in the null-field integral formulation. By collocating the null-field point exactly on the real boundary and matching the boundary condition, the linear algebraic system is obtained and the unknown Fourier coefficients can be easily determined. Then, series solutions for the warping function, torsional rigidity and stress are obtained. Convergence study is also addressed. Numerical examples are given to show the validity and efficiency of our formulation.

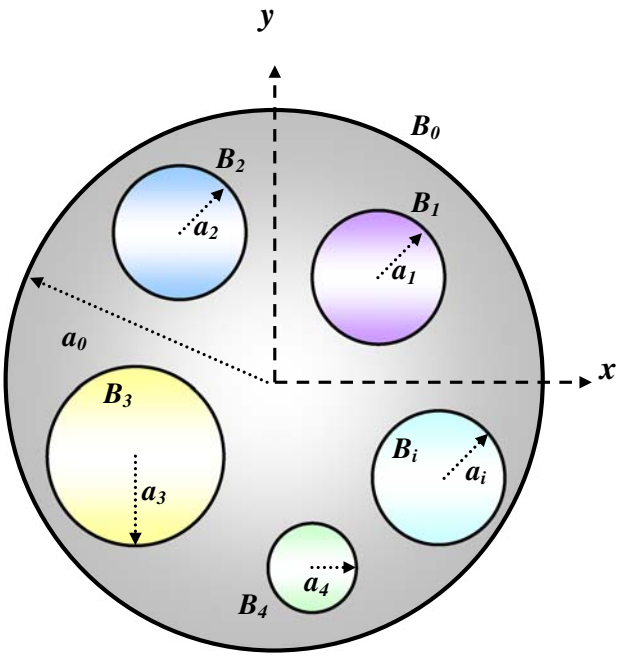

Fig. 1 Sketch of a *circular bar* with circular inclusions and/or *holes* under torsion

2 Formulation of the problem

A circular bar containing N circular inclusions bounded to the contours B_k $(k = 0, 1, 2, \ldots, N)$ is shown in Fig. 1. We define

$$B = \bigcup_{k=0}^{N} B_k. \tag{1}$$

The radii of circular bar and inclusions are a_0 and $a_i (i = 1, 2, \ldots, N)$, respectively. The circular bar twisted by couples applied at the end is taken into consideration. Following the theory of Saint-Venant torsion [28], we assume the displacement to be

$$u = -\alpha yz, \quad v = \alpha xz, \quad w = \alpha\varphi(x, y), \tag{2}$$

where α is the angle of twist per unit length along the z direction and φ is the warping function. The relation of strain and displacement is defined in the elasticity book [28] as shown below:

$$\begin{aligned} \varepsilon_x &= \frac{\partial u}{\partial x}, \quad \gamma_{xy} = \frac{\partial u}{\partial y} + \frac{\partial v}{\partial x}, \\ \varepsilon_y &= \frac{\partial v}{\partial y}, \quad \gamma_{yz} = \frac{\partial v}{\partial z} + \frac{\partial w}{\partial y}, \\ \varepsilon_z &= \frac{\partial w}{\partial z}, \quad \gamma_{zx} = \frac{\partial w}{\partial x} + \frac{\partial u}{\partial z}. \end{aligned} \tag{3}$$

Then, substituting the displacement of Eq. 2 into Eq. 3, we have the strain components as follows:

$$\begin{aligned}
&\varepsilon_x = \varepsilon_y = \varepsilon_z = \gamma_{xy} = 0,\\
&\gamma_{xz} = \alpha\left(\frac{\partial\varphi}{\partial x} - y\right),\\
&\gamma_{yz} = \alpha\left(\frac{\partial\varphi}{\partial y} + x\right).
\end{aligned} \tag{4}$$

By applying the Hooke's law, the stress components are

$$\begin{aligned}
&\sigma_x = \sigma_y = \sigma_z = \sigma_{xy} = 0,\\
&\sigma_{xz} = \mu\alpha\left(\frac{\partial\varphi}{\partial x} - y\right),\\
&\sigma_{yz} = \mu\alpha\left(\frac{\partial\varphi}{\partial y} + x\right),
\end{aligned} \tag{5}$$

where μ is the shear modulus. There is no distortion in the planes of cross sections since $\varepsilon_x = \varepsilon_y = \varepsilon_z = \gamma_{xy} = 0$. We have the state of pure shear at each point defined by the stress components σ_{xz} and σ_{yz}. By substituting Eq. 5 to the equilibrium equation

$$\begin{aligned}
&\frac{\partial\sigma_x}{\partial x} + \frac{\partial\sigma_{xy}}{\partial y} + \frac{\partial\sigma_{xz}}{\partial z} + F_x = 0,\\
&\frac{\partial\sigma_y}{\partial y} + \frac{\partial\sigma_{xy}}{\partial x} + \frac{\partial\sigma_{yz}}{\partial z} + F_y = 0,\\
&\frac{\partial\sigma_z}{\partial z} + \frac{\partial\sigma_{xz}}{\partial x} + \frac{\partial\sigma_{yz}}{\partial y} + F_z = 0,
\end{aligned} \tag{6}$$

the warping function satisfies the Laplace equation

$$\frac{\partial^2\varphi}{\partial x^2} + \frac{\partial^2\varphi}{\partial y^2} = 0 \quad \text{in } D, \tag{7}$$

where the body forces (F_x, F_y and F_z) are neglected and D is the domain of interest. On the cylinder surface, the stress states in Eq. 5 result in zero traction of $t_x = t_y = 0$. The only nonzero traction is t_z. Since there is no external traction, t_z, on the cylindrical surface, we have

$$\begin{aligned}
t_z &= \sigma_{xz}n_x + \sigma_{yz}n_y\\
&= \mu\alpha\left(\frac{\partial\varphi}{\partial x}n_x + \frac{\partial\varphi}{\partial y}n_y - yn_x + xn_y\right) = 0.
\end{aligned} \tag{8}$$

Therefore, the bracket in Eq. 8 is equal to zero and we have the boundary condition as follows:

$$\frac{\partial\varphi}{\partial x}n_x + \frac{\partial\varphi}{\partial y}n_y = \nabla\varphi\cdot\mathbf{n} = \frac{\partial\varphi}{\partial n} = yn_x - xn_y. \tag{9}$$

For the ideal boundary between the matrix and inclusions, the continuity condition for the displacement and equilibrium condition for traction on the interface [19] yield:

$$\varphi^M = \varphi^I \quad \text{on } B_i, \tag{10}$$

$$\mu_0\frac{\partial\varphi_i^M}{\partial n} - \mu_i\frac{\partial\varphi_i^I}{\partial y} = (\mu_0 - \mu_i)(yn_x - xn_y) \quad \text{on } B_i, \tag{11}$$

where the superscripts "I" and "M" denote the inclusion and matrix, respectively, B_i is the ith interface boundary, μ_0 is the shear modulus for the matrix and μ_i is the shear modulus for the ith inclusion.

3 Method of solution

3.1 Dual null-field integral equations—the conventional version

The integral equation for the domain point can be derived from the third Green's identity [6], we have

$$\begin{aligned}
2\pi\varphi(x) &= \int_B T(s,x)\varphi(s)\,\mathrm{d}B(s)\\
&\quad - \int_B U(s,x)\psi(s)\,\mathrm{d}B(s), \quad x \in D,
\end{aligned} \tag{12}$$

$$\begin{aligned}
2\pi\frac{\partial\varphi(x)}{\partial n_x} &= \int_B M(s,x)\varphi(s)\,\mathrm{d}B(s)\\
&\quad - \int_B L(s,x)\psi(s)\,\mathrm{d}B(s), \quad x \in D,
\end{aligned} \tag{13}$$

where s and x are the source and field points, respectively, D is the domain of interest, $\psi(s) = \frac{\partial\varphi(s)}{\partial n_s}$, n_s and n_x denote the outward normal vectors at the source point s and field point x, respectively, and the kernel function $U(s,x) = \ln r$, $(r \equiv |s - x|)$, is the fundamental solution which satisfies

$$\nabla^2 U(s,x) = 2\pi\delta(x - s) \tag{14}$$

in which $\delta(x-s)$ denotes the Dirac-delta function. The other kernel functions, $T(s,x)$, $L(s,x)$, and $M(s,x)$, are defined by

$$T(s,x) = \frac{\partial U(s,x)}{\partial n_s}, \tag{15}$$

$$L(s,x) = \frac{\partial U(s,x)}{\partial n_x}, \tag{16}$$

$$M(s,x) = \frac{\partial^2 U(s,x)}{\partial n_s \partial n_x}. \tag{17}$$

By moving the field point to the boundary, Eqs. 12 and 13 reduce to

$$\pi\varphi(x) = C.P.V.\int_B T(s,x)\varphi(s)\,\mathrm{d}B(s) - R.P.V.\int_B U(s,x)\psi(s)\,\mathrm{d}B(s), \quad x \in B, \tag{18}$$

$$\pi\frac{\partial\varphi(x)}{\partial n_x} = H.P.V.\int_B M(s,x)\varphi(s)\,\mathrm{d}B(s) - C.P.V.\int_B L(s,x)\psi(s)\,\mathrm{d}B(s), \quad x \in B, \tag{19}$$

where $R.P.V.$, $C.P.V.$ and $H.P.V.$ denote the Riemann principal value, Cauchy principal value and Hadamard principal value, respectively. Once the field point x locates outside the domain ($x \in D^c$), we obtain the dual null-field integral equations as shown below

$$0 = \int_B T(s,x)\varphi(s)\,\mathrm{d}B(s) - \int_B U(s,x)\psi(s)\,\mathrm{d}B(s), \quad x \in D^c, \tag{20}$$

$$0 = \int_B M(s,x)\varphi(s)\,\mathrm{d}B(s) - \int_B L(s,x)\psi(s)\,\mathrm{d}B(s), \quad x \in D^c, \tag{21}$$

where D^c is the complementary domain. Equations 12, 13, 20 and 21 are conventional formulations where the point can not be located on the real boundary. Singularity occurs and concept of principal values is required once Eqs. 18 and 19 are considered.

3.2 Dual null-field integral formulation—the present version

By introducing the degenerate kernels, the collocation point can be located on the real boundary free of facing singularity. Therefore, the representations of integral equations including the boundary point for the interior problem can be written as

$$2\pi\varphi(x) = \int_B T^i(s,x)\varphi(s)\,\mathrm{d}B(s) - \int_B U^i(s,x)\psi(s)\,\mathrm{d}B(s), \quad x \in D \cup B, \tag{22}$$

$$2\pi\frac{\partial\varphi(x)}{\partial n_x} = \int_B M^i(s,x)\varphi(s)\,\mathrm{d}B(s) - \int_B L^i(s,x)\psi(s)\,\mathrm{d}B(s), \quad x \in D \cup B, \tag{23}$$

and

$$0 = \int_B T^e(s,x)\varphi(s)\,\mathrm{d}B(s) - \int_B U^e(s,x)\psi(s)\,\mathrm{d}B(s), \quad x \in D^c \cup B, \tag{24}$$

$$0 = \int_B M^e(s,x)\varphi(s)\,\mathrm{d}B(s) - \int_B L^e(s,x)\psi(s)\,\mathrm{d}B(s), \quad x \in D^c \cup B, \tag{25}$$

once the kernels are expressed in term of an appropriate degenerate forms (denoted by subscripts i and e) instead of the closed-form fundamental solution without distinction. It is noted that x in Eqs. 22–25 can exactly be located on the real boundary. For the exterior problem, the domain of interest is in the external region of the circular boundary and the complementary domain is in the internal region of the circle. Therefore, the null-field integral equations are represented as

$$2\pi\varphi(x) = \int_B T^e(s,x)\varphi(s)\,\mathrm{d}B(s) - \int_B U^e(s,x)\psi(s)\,\mathrm{d}B(s), \quad x \in D \cup B, \tag{26}$$

$$2\pi\frac{\partial\varphi(x)}{\partial n_x} = \int_B M^e(s,x)\varphi(s)\,\mathrm{d}B(s) - \int_B L^e(s,x)\psi(s)\,\mathrm{d}B(s), \quad x \in D \cup B, \tag{27}$$

and

$$0 = \int_B T^i(s,x)\varphi(s)\,\mathrm{d}B(s) - \int_B U^i(s,x)\psi(s)\,\mathrm{d}B(s), \quad x \in D^c \cup B, \tag{28}$$

$$0 = \int_B M^i(s,x)\varphi(s)\,\mathrm{d}B(s) - \int_B L^i(s,x)\psi(s)\,\mathrm{d}B(s), \quad x \in D^c \cup B, \tag{29}$$

Also, x in Eqs. 26–29 can exactly be located on the real boundary. For various problems (interior or exterior), we used different kernel functions (denoted by superscripts "i"

and "e") so that jump behavior across the boundary can be captured. Therefore, different expressions of the kernels for the interior and exterior observer points are used and they will be elaborated on latter.

It is worthy of noting that our approach can yield the same linear algebraic equation derived from boundary integral equation in Eqs. 18 and 19. However, the procedure is quite different although collocation points are located on the real boundary for both the conventional BIEM and the present approach. For the conventional BEM, it is necessary to calculate the singular or hypersingular integral by using the sense of principal value. Our approach is free of calculating principal value due to the introduction of the degenerate kernel since the kernel functions were separated into two parts, interior and exterior parts. If the appropriate kernels (interior and exterior parts) are chosen, we can easily obtain the same linear algebraic equation derived from the conventional BIE and free of calculating principal value.

3.3 Expansions of fundamental solution and boundary density

Based on the separable property, the kernel function $U(s,x)$ can be expanded into degenerate form by separating the source points and field points in the polar coordinates [5]:

$$U(s,x) = \begin{cases} U^i(R,\theta;\rho,\phi) = \ln R - \sum_{m=1}^{\infty} \frac{1}{m}\left(\frac{\rho}{R}\right)^m \cos m(\theta-\phi), \\ \qquad R \geq \rho, \\ U^e(R,\theta;\rho,\phi) = \ln \rho - \sum_{m=1}^{\infty} \frac{1}{m}\left(\frac{R}{\rho}\right)^m \cos m(\theta-\phi), \\ \qquad R < \rho, \end{cases} \tag{30}$$

where the superscripts "i" and "e" denote the interior ($R \geq \rho$) and exterior ($R < \rho$) cases, respectively. In order to ensure the log singularity and the series convergence, the leading term and the numerator in the above expansion is dominated by the larger argument. After taking the derivative operators in Eqs. 15-17, $T(s,x)$, $L(s,x)$ and $M(s,x)$ kernels can be easily derived and the detailed representation can be found in [7]. It is noted that the null-field point or the domain point can be exactly located on the real boundary when the appropriate degenerate kernels are employed. The main advantage of present formulation is that the collocation point x is located on the real boundary free of singular integrals, while the conventional BEM needs to deal with singularities since a closed-form kernel is used. Therefore, the main difference between our approach and the conventional method is that we don't use the bump contour approach on the integration path to obtain free term. Furthermore, the jump behavior for potentials of integral equations between the domain point and the null-field point is captured when various degenerate kernels for fundamental solutions are employed for the domain point and complementary domain point. In other words, the jump behavior is revealed by using various degenerate kernels for the fundamental solution instead of employing the bump contour approach in the conventional boundary integral equation method.

For the boundary densities, we apply the Fourier series expansions to approximate the potential φ and its normal derivative ψ on the boundary

$$\varphi(s_k) = a_0^k + \sum_{n=1}^{\infty} (a_n^k \cos n\theta + b_n^k \sin n\theta), \quad s_k \in B_k, \quad k = 1, 2, \ldots, N, \tag{31}$$

$$\psi(s_k) = p_0^k + \sum_{n=1}^{\infty} (p_n^k \cos n\theta + q_n^k \sin n\theta), \quad s_k \in B_k, \quad k = 1, 2, \ldots, N, \tag{32}$$

where a_n^k, b_n^k, p_n^k and q_n^k are the Fourier coefficients and θ is the polar angle ($0 < \theta < 2\pi$).

3.4 Linear algebraic system

After locating the null-field point x_k exactly on the kth circular boundary in Eq. 24 or Eq. 28 as shown in Fig. 2, we have

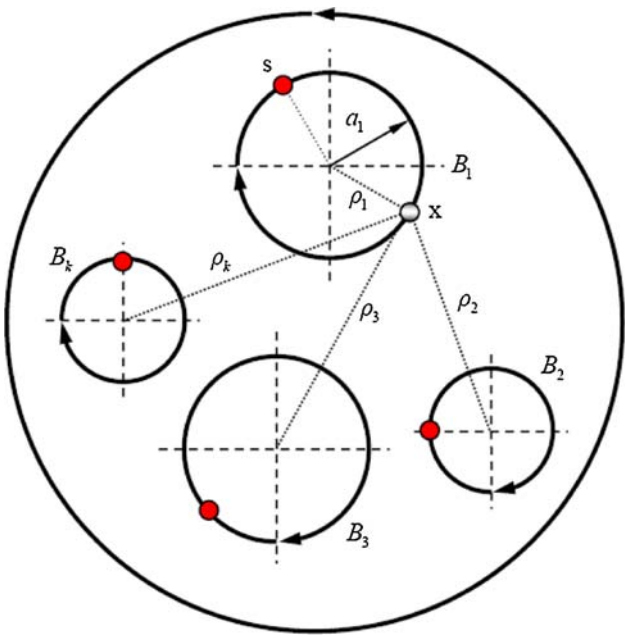

Fig. 2 Sketch of the null-field integral equation in conjunction with the adaptive observer system

$$0 = \sum_{k=0}^{N} \int_{B_k} T(s,x)\varphi(s)\,\mathrm{d}B_k(s) - \sum_{k=0}^{N} \int_{B_k} U(s,x)\psi(s)\,\mathrm{d}B_k(s), \quad x \in D^c \cup B, \tag{33}$$

where N is the number of circles including the outer boundary and the inner circular holes. Since the boundary integral equations are frame indifferent, i.e. objectivity rule is satisfied. The origin of observer system is adaptively chosen at the center of circular boundary under integration. The dummy variable in the circular integration is angle (θ) instead of radial coordinate (R). In the real computation, we select the collocation point on the boundary and the integration path is counterclockwise for the outer circle. Otherwise, it is clockwise. For the B integral of the circular boundary, the kernels of $U(s,x)$ and $T(s,x)$ are expressed in terms of degenerate kernels, and $\varphi(s)$ and $\psi(s)$ are substituted by using the Fourier series. In the B_k integral, we set the origin of the observer system to collocate at the center c_k to fully utilize the degenerate kernels and Fourier series. By collocating the null-field point exactly on the boundary, a linear algebraic system is obtained

$$[\mathbf{U}]\{\psi\} = [\mathbf{T}]\{\varphi\}, \tag{34}$$

where $[\mathbf{U}]$ and $[\mathbf{T}]$ are the influence matrices with a dimension of $N \times (2L+1)$ by $N \times (2L+1)$, $\{\varphi\}$ and $\{\psi\}$ denote the column vectors of Fourier coefficients with a dimension of $N \times (2L+1)$ by 1 in which $[\mathbf{U}]$, $[\mathbf{T}]$, $\{\varphi\}$ and $\{\psi\}$ can be defined as follows:

$$[\mathbf{U}] = \begin{bmatrix} \mathbf{U}_{00} & \mathbf{U}_{01} & \dots & \mathbf{U}_{0N} \\ \mathbf{U}_{10} & \mathbf{U}_{11} & \dots & \mathbf{U}_{1N} \\ \vdots & \vdots & \ddots & \vdots \\ \mathbf{U}_{N0} & \mathbf{U}_{N0} & \dots & \mathbf{U}_{NN} \end{bmatrix}, \tag{35}$$

$$[\mathbf{T}] = \begin{bmatrix} \mathbf{T}_{00} & \mathbf{T}_{01} & \dots & \mathbf{T}_{0N} \\ \mathbf{T}_{10} & \mathbf{T}_{NN} & \dots & \mathbf{T}_{1N} \\ \vdots & \vdots & \ddots & \vdots \\ \mathbf{T}_{N0} & \mathbf{T}_{N1} & \dots & \mathbf{T}_{NN} \end{bmatrix}, \tag{36}$$

$$\{\varphi\} = \begin{Bmatrix} \varphi_0 \\ \varphi_1 \\ \varphi_2 \\ \vdots \\ \varphi_N \end{Bmatrix}, \quad \{\psi\} = \begin{Bmatrix} \psi_0 \\ \psi_1 \\ \psi_2 \\ \vdots \\ \psi_N \end{Bmatrix} \tag{37}$$

where the vectors $\{\varphi_k\}$ and $\{\psi_k\}$ are in the forms of $\{a_0^k a_1^k b_1^k \dots a_L^k b_L^k\}^T$ and $\{p_0^k p_1^k q_1^k \dots p_L^k q_L^k\}^T$, respectively; the first subscript "j" ($j = 0, 1, 2, \dots, N,$) in $[\mathbf{U}_{jk}]$ and $[\mathbf{T}_{jk}]$ denotes the index of the jth circle where the collocation point is located and the second subscript "k" ($k = 0, 1, 2, \dots, N,$) denotes the index of the kth circle where the boundary data $\{\varphi_k\}$ and $\{\psi_k\}$ are specified and L indicates the truncated terms of Fourier series. The coefficient matrix of the linear algebraic system is partitioned into blocks, and each off-diagonal block corresponds to the influence matrices between two different circular holes. The diagonal blocks are the influence matrices due to itself in each individual hole. After uniformly collocating the null-field point along the kth circular boundary, the submatrix can be written as

$$[\mathbf{K}_{jk}] = \begin{bmatrix} K_{jk}^{0c}(\phi_1) & K_{jk}^{1c}(\phi_1) & K_{jk}^{1s}(\phi_1) & \dots & K_{jk}^{Lc}(\phi_1) & K_{jk}^{Ls}(\phi_1) \\ K_{jk}^{0c}(\phi_2) & K_{jk}^{1c}(\phi_2) & K_{jk}^{1s}(\phi_2) & \dots & K_{jk}^{Lc}(\phi_2) & K_{jk}^{Ls}(\phi_2) \\ K_{jk}^{0c}(\phi_3) & K_{jk}^{1c}(\phi_3) & K_{jk}^{1s}(\phi_3) & \dots & K_{jk}^{Lc}(\phi_3) & K_{jk}^{Ls}(\phi_3) \\ \vdots & \vdots & \vdots & \ddots & \vdots & \vdots \\ K_{jk}^{0c}(\phi_{2L}) & K_{jk}^{1c}(\phi_{2L}) & K_{jk}^{1s}(\phi_{2L}) & \dots & K_{jk}^{Lc}(\phi_{2L}) & K_{jk}^{Ls}(\phi_{2L}) \\ K_{jk}^{0c}(\phi_{2L+1}) & K_{jk}^{1c}(\phi_{2L+1}) & K_{jk}^{1s}(\phi_{2L+1}) & \dots & K_{jk}^{Lc}(\phi_{2L+1}) & K_{jk}^{Ls}(\phi_{2L+1}) \end{bmatrix}, \tag{38}$$

where K can be substituted by U or T. Although the matrix in Eq. 38 is not sparse, it is diagonally dominant. It is found that the influence coefficient for the higher-order harmonics is smaller. It is noted that the superscript "0s" in Eq. 38 disappears since $\sin(0\theta) = 0$. The element of $[\mathbf{K}_{jk}]$ is defined, respectively, as

$$K_{jk}^{nc}(\phi_m) = \int_{B_k} K(s_k, x_m)\cos(n\theta_k) R_k d\theta_k, \tag{39}$$

$$K_{jk}^{ns}(\phi_m) = \int_{B_k} K(s_k, x_m)\sin(n\theta_k) R_k d\theta_k, \tag{40}$$

where $n = 0, 1, 2, \dots, L$, $m = 1, 2, \dots, 2L+1$, and ϕ_m is the polar angle of the collocating points x_m along the boundary. The physical meaning of the influence coefficient for $U_{jk}^{nc}(\phi_m)$ in Eq. 39 denotes the response at x_m due to the $\cos(n\theta)$ distribution. By rearranging the known and unknown sets, the unknown Fourier coefficients are determined. Equation 24 can be calculated by employing the orthogonal relations of trigonometric functions in the real computation.

Only the finite L terms are used in the summation of Eqs. 31 and 32.

By using the concept of domain decomposition, the problem in Fig. 1 can be decomposed into two parts as shown in Figs. 3(a) and 3(b). One is the torsion problem of a circular bar with multiple circular holes and the other is a problem of each inclusion. For the torsion problem with circular holes which satisfies the Laplace equation, the linear algebraic system from Eq. 34 can be obtained as

$$\begin{bmatrix} \mathbf{T}_{00}^M & \mathbf{T}_{01}^M & \cdots & \mathbf{T}_{0N}^M & -\mathbf{U}_{01}^M & \cdots & -\mathbf{U}_{0N}^M \\ \mathbf{T}_{10}^M & \mathbf{T}_{11}^M & \cdots & \mathbf{T}_{1N}^M & -\mathbf{U}_{11}^M & \cdots & -\mathbf{U}_{1N}^M \\ \vdots & \vdots & \ddots & \vdots & \vdots & \ddots & \vdots \\ \mathbf{T}_{N0}^M & \mathbf{T}_{N1}^M & \cdots & \mathbf{T}_{NN}^M & -\mathbf{U}_{N1}^M & \cdots & -\mathbf{U}_{NN}^M \end{bmatrix} \begin{Bmatrix} \varphi_0^M \\ \varphi_1^M \\ \vdots \\ \varphi_N^M \\ \psi_1^M \\ \vdots \\ \psi_N^M \end{Bmatrix} = \begin{Bmatrix} \mathbf{0} \\ \mathbf{0} \\ \vdots \\ \mathbf{0} \end{Bmatrix}. \tag{41}$$

For each inclusion, we have

$$\begin{bmatrix} \mathbf{T}_{11}^I & \mathbf{0} & \mathbf{0} & -\mathbf{U}_{11}^I & \mathbf{0} & \mathbf{0} \\ \mathbf{0} & \ddots & \mathbf{0} & \mathbf{0} & \ddots & \mathbf{0} \\ \mathbf{0} & \mathbf{0} & \mathbf{T}_{NN}^I & \mathbf{0} & \mathbf{0} & -\mathbf{U}_{NN}^I \end{bmatrix} \begin{Bmatrix} \varphi_1^I \\ \vdots \\ \varphi_N^I \\ \psi_1^I \\ \vdots \\ \psi_N^I \end{Bmatrix} = \begin{Bmatrix} \mathbf{0} \\ \vdots \\ \mathbf{0} \end{Bmatrix}. \tag{42}$$

In order to satisfy the continuity conditions of displacement and equilibrium condition of traction on the interface, we have

$$\left\{\varphi_i^M\right\} - \left\{\varphi_i^I\right\} = \{\mathbf{0}\}, \tag{43}$$

$$\mu_0 \left\{\psi_i^M\right\} - \mu_i \left\{\psi_i^I\right\} = \left\{\mathbf{b}^i\right\}, \tag{44}$$

where $\{\mathbf{b}^i\}$ is

$$\left\{\mathbf{b}^i\right\} = \begin{Bmatrix} (\mu_0 - \mu_i)(e_y^i \cos\theta_1^i - e_x^i \sin\theta_1^i) \\ (\mu_0 - \mu_i)(e_y^i \cos\theta_2^i - e_x^i \sin\theta_2^i) \\ \vdots \\ (\mu_0 - \mu_i)(e_y^i \cos\theta_{2L}^i - e_x^i \sin\theta_{2L}^i) \\ (\mu_0 - \mu_i)(e_y^i \cos\theta_{2L+1}^i - e_x^i \sin\theta_{2L+1}^i) \end{Bmatrix}. \tag{45}$$

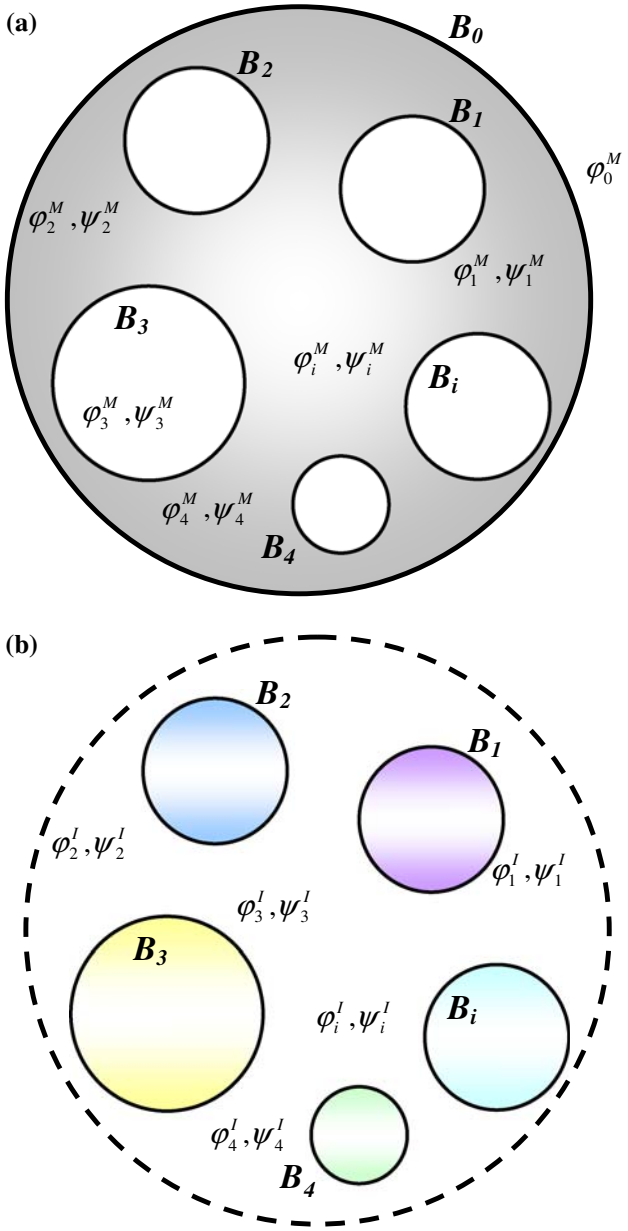

Fig. 3 **a** Torsion problem of a circular bar with circular holes. **b** Each circular inclusion problem

Combining with the above mentioned linear algebraic system of Eqs. 41–44, the global linear algebraic equation is obtained by correctly arranging the Fourier coefficients. After obtaining the Fourier coefficients, the torsional rigidity can be easily determined as follows:

$$G = \mu \int_D (x^2 + y^2) dD - \mu \sum_{k=1}^{N} \int_{B_k} \varphi \frac{\partial \varphi}{\partial n} dB_k, \tag{46}$$

$$G^T = G^M + G^I, \tag{47}$$

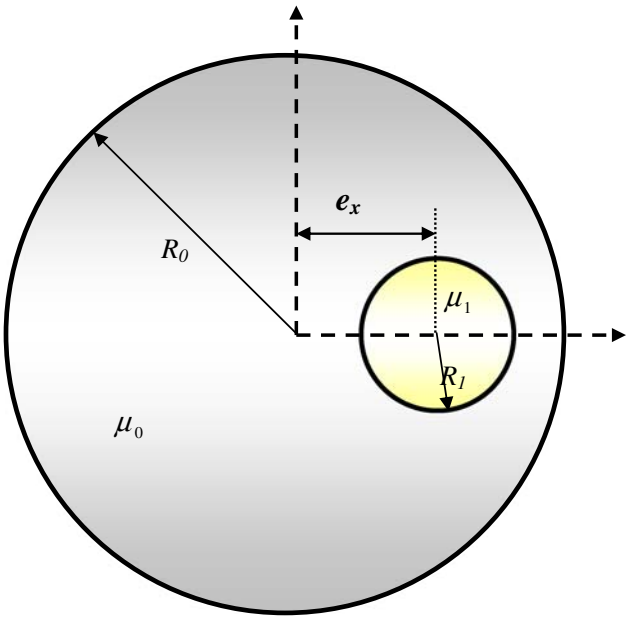

Fig. 4 Sketch of an eccentric circular inclusion problem

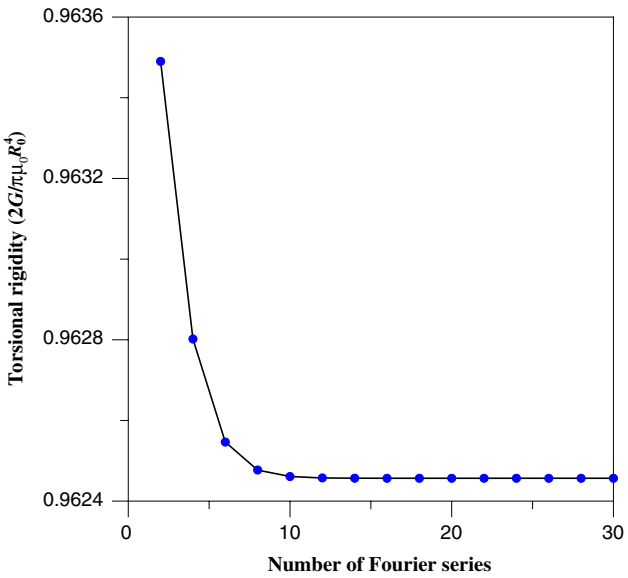

Fig. 5 Torsional rigidity versus the number of Fourier series terms

where the subscripts of "T", "M" and "I" denote the torsion rigidity of total, matrix and inclusion, respectively.

4 Illustrative examples and discussions

In this section, we revisit the torsion problems with inclusions and/or holes which have been solved by Muskhelishvili [19], Petrov [21], Tang [27], Ling [14], and Kuo and Conway [12,13] for demonstrating the validity of present method. The torsional rigidity of each example is calculated after determining the unknown Fourier coefficients.

Example 1 A circular bar with an eccentric inclusion.

A circular bar of radius R_0 with an eccentric circular inclusion of radius R_1 is shown in Fig. 4. The ratio of R_1/R_0 and e_x/R_0 are 0.3 and 0.6, respectively. Fig. 5 shows the torsional rigidity versus the number of Fourier series term when μ_1/μ_0 is equal to 0.6. It is found that the solution converges fast by using only fourteen terms of Fourier series. The results of torsional rigidity for different values of μ_1/μ_0 are shown in Table 1. For verifying our results, the Muskhelishvili's solution [19] is shown below,

$$G = \mu_0 I + (\mu_1 - \mu_0) I' - \frac{\pi R_1^2 e_x^2 (\mu_1 - \mu_0)^2}{\mu_1 + \mu_0} - 2\mu_0 \pi e_x^2 \nu \rho_1^2 \sum_{k=1}^{\infty} \frac{\alpha^k \nu^k}{(1 - a^2 \rho_1^2 \alpha^k)^2}, \tag{48}$$

where $I = (\pi R_0^4/2)$, $I' = (\pi R_1^4/2) + \pi R_1^2 e_x^2$, $a = e_x/(\sqrt{(R_1^2 - R_0^2)^2 - 2e_x^2(R_1^2 + R_0^2) + e_x^4})$, $\alpha = (\rho_1^2/\rho_0^2)$, $\nu = ((\mu_0 - \mu_1)/(\mu_0 + \mu_1))$, $\rho_1 = (\sqrt{1 + 4R_1^2 a^2} - 1/2R_1 a^2)$ and $\rho_0 = (\sqrt{1 + 4R_0^2 a^2} - 1/2R_0 a^2)$. The exact solution of Muskhelishvili and the result of integral formulation by Tang [27] are shown in Table 1 for comparison. The present results match very well with the exact solution derived by Muskhelishvil and are better than those of Tang [27]. For the rigid inclusion, the torsional rigidity becomes infinity as shown in Table 1. Fig. 6 is shown to indicate how shear modulus of inclusion influences the torsional rigidity. It is observed that the slope of torsional rigidity versus μ_1 is $(R_1/R_0)^4$ when the shear modulus of the inclusion becomes large. This finding is expected according to Eq. 44.

Example 2 A circular bar with one circular hole (limiting case).

The problem is different from the Case 1 by setting zero modulus of the inclusion to simulate the hole in our program. The limiting case is used to check the present formulation. The radius of a circular bar is 1.0 and the radius of the hole is 0.3. The eccentricity ($e_x = 0.5$) is considered. The shear moduli μ_0 and μ_1 are chosen 1.0 and 0, respectively. The exact solution of Muskhelishvili [19] is also calculated by using the exact formula. The results are shown in Table 2. It is found that the results of present method matches well with those of the Muskhelishvili's data [19] and are better than those of the Petrov's results [21]. However, the Lurje's solution [15] is smaller than those of the Petrov's, Muskhelishvili's and our results. Since three various

Table 1 Torsional rigidity of a circular bar with an eccentric inclusion

$\frac{\mu_1}{\mu_0}$	$2G/\pi\mu_0 R_0^4$		
	Muskhelishvili [19]	Tang [27]	Present method ($M = 20$)
0	0.82370	0.82377	0.82370
0.2	0.89180	0.89181	0.89180
0.6	0.96246	0.96246	0.96246
1.0	1.00000	1.00000	1.00000
5.0	1.10800	1.10794	1.10800
20.0	1.25224	1.25181	1.25224
1000	9.19866	N/A	9.19866
10000	82.09883	N/A	82.09882
1000000	8101.10012	N/A	8101.09883

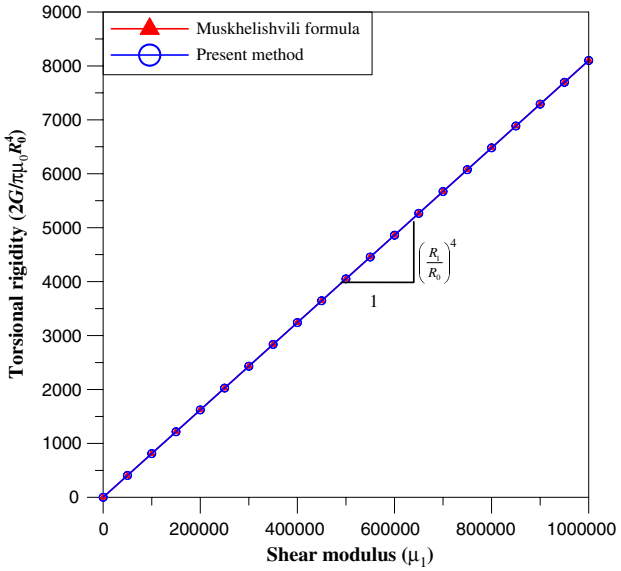

Fig. 6 Torsional rigidity versus the shear modulus of inclusion

Table 2 Torsional rigidity of a circular bar with an eccentric hole

	$G/\mu_0 R_0^4$		
Present method	1.389 (34)	1.389 (66)	1.389 (130)
Petrov [21]	1.391 (32)	1.390 (64)	1.389 (130)
Lurje [15]	1.311		
Muskhelishvili [19]	1.389		

The data in the parenthesis denotes number of degrees of freedom

methods obtain the consistent result, the formulae of Lurje [15] needs further check.

The stress analysis has been done by Ling [14]. The corresponding parameters are shown in Fig. 7. The definition of shear stress component, ξ_z, is shown below

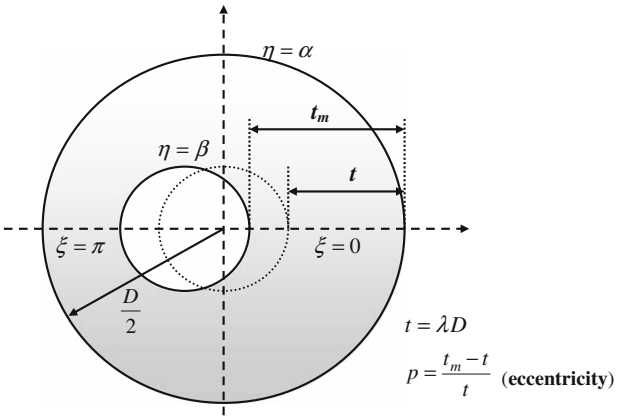

Fig. 7 Sketch of eccentric problem

$$\xi_z = \mu_0 \alpha \frac{\partial \varphi}{\partial \eta}. \tag{49}$$

By using the chain rule, we can obtain the following relation

$$\xi_z = \mu_0 \alpha \left(\frac{\partial \varphi}{\partial x}\frac{\partial x}{\partial \eta} + \frac{\partial \varphi}{\partial y}\frac{\partial y}{\partial \eta} \right), \tag{50}$$

where $x = \frac{a \sinh \eta}{\cosh \eta - \cos \xi}$, $y = \frac{a \sin \xi}{\cosh \eta - \cos \xi}$ and a in our case is 1.58016. The stresses along the inner and outer boundaries for $\lambda = 0.3$ and $p = 0.4$ are shown in Table 3. It is found that the errors are less than two percents. The stresses on the x axis in domain are shown in Table 4. The results are very close to the Ling's analytical results obtained from the bipolar coordinate system.

Example 3 A circular rod with a ring of circular inclusions.

In this example, we revisit the problems of a circular rod with a ring of circular inclusions investigated by Kuo and Conway [12] as shown in Fig. 8. Three cases are given in their article as

Case 1: $\frac{b}{a} = \frac{3}{4}, \frac{\lambda}{a} = \frac{1}{8}, \frac{\delta}{a} = \frac{1}{2}, \frac{G_2}{G_1} = 30, k = 8,$
Case 2: $\frac{b}{a} = \frac{3}{4}, \frac{\lambda}{a} = \frac{1}{8}, \frac{\delta}{a} = \frac{1}{2}, \frac{G_2}{G_1} = 5, k = 3,$
Case 3: $\frac{b}{a} = \frac{1}{2}, \frac{\lambda}{a} = \frac{1}{4}, \frac{\delta}{a} = 0, \frac{G_2}{G_1} = 29.4, k = 4.$

The results of the present approach are shown in Table 5. It is found that the results of our approach are slightly different from the Kuo and Conway's results. For the Case 3, Kuo and Conway [12] claimed that they obtained the nondimensional torsional rigidity 1.57 analytically and 1.53 in the experiment. It seems that they obtained consistent results. However, the data of FE solution 1.77 obtained by Murakami and Yamakawa [18] agrees well with the result of our approach. In this case, our result deviates from the experiment data of Kuo and Conway [12] but converges to the data of finer mesh using FEM by Murakami and Yamakawa [18]. Both our result and that of Murakami and Yamakawa

Table 3 ξ_z on the boundary for $\lambda = 0.3$ and $p = 0.4$

ξ	$\eta = \alpha$			$\eta = \beta$		
	θ	$\frac{2}{\mu\tau D}\xi_z$[14]	Present method	θ	$\frac{2}{\mu\tau D}\xi_z$[14]	Present method
π	180°	1.166	1.166	180°	1.015	1.012
$\frac{3}{4}\pi$	154°18′	1.115	1.114	144°16′	0.881	0.881
$\frac{1}{2}\pi$	122°19′	1.011	1.011	104°12′	0.522	0.522
$\frac{1}{4}\pi$	73°55′	0.949	0.949	56°2′	0.068	0.067
0	0°	0.936	0.940	0°	−0.166	−0.167

Table 4 ξ_z along the line of $\xi = 0$ and π for $\lambda = 0.3$ and $p = 0.4$

η	$\xi = \pi$			$\xi = 0$		
	$\frac{x_1}{D}$	$\frac{2}{\mu\tau D}\xi_z$[14]	Present method	$\frac{x_2}{D}$	$\frac{2}{\mu\tau D}\xi_z$[14]	Present method
1.2384	0	1.166	1.166	0	0.940	0.940
1.4084	0.0446	1.097	1.096	0.1335	0.652	0.651
1.5784	0.0848	1.044	1.043	0.2342	0.420	0.418
1.7484	0.1208	1.009	1.010	0.3120	0.215	0.216
1.9784	0.1528	0.998	0.999	0.3730	0.026	0.026
2.0826	0.1800	1.015	1.012	0.4200	−0.166	−0.167

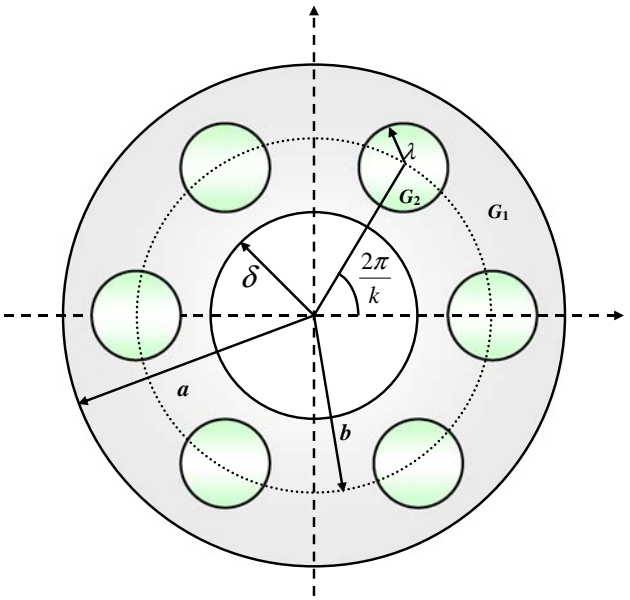

Fig. 8 A *circular rod* with a *ring* of circular inclusions

may open the issue that Kuo and Conway's result may be questionable. In general, the numerical analysis is developed to predict the data before experiment. However, we always find that the results have differences between the numerical analysis and experiment data. We may wonder that the numerical result may not be correct if the two results deviate. As we know, the mathematical model is established under certain assumptions. Therefore, the mathematical model is always simpler than the real problem. If the mathematical model has the analytical or exact solution, it is the basic solution for comparison with the numerical result. For the real problem, many uncertain conditions exist in the experiment. Valid experimental data need special care. The inconsistency between the experimental data and numerical results stems from many reasons. So, the mathematical model is continuously modified by adding specific consideration.

Example 4 A *circular rod* with several *rings* of circular inclusions.

In this example, we consider a circular rod with several rings of circular inclusions proposed by Kuo and Conway [13]. Four cases were addressed

Case 1: $\frac{b_1}{a} = \frac{3}{8}, \frac{b_2}{a} = \frac{3}{4}, \frac{\lambda}{a} = \frac{1}{8}, \frac{G}{G_0} = 30, j = 2, k = 6,$

Case 2: $\frac{b_1}{a} = \frac{1}{4}, \frac{b_2}{a} = \frac{17}{32}, \frac{b_3}{a} = \frac{13}{16}, \frac{\lambda}{a} = \frac{3}{32}, \frac{G}{G_0} = 30,$
$j = 3, k = 6,$

Case 3: $\frac{b_1}{a} = \frac{3}{8}, \frac{b_2}{a} = \frac{3}{4}, \frac{\lambda}{a} = \frac{1}{8}, \frac{G}{G_0} = 0, j = 2, k = 6,$

Case 4: $\frac{b_1}{a} = \frac{1}{4}, \frac{b_2}{a} = \frac{17}{32}, \frac{b_3}{a} = \frac{13}{16}, \frac{\lambda}{a} = \frac{3}{32}, \frac{G}{G_0} = 0,$
$j = 3, k = 6.$

Table 5 Torsional rigidity of different cases for a circular ring with inclusions

Case	$\frac{b}{a}$	$\frac{\lambda}{a}$	$\frac{\delta}{a}$	$\frac{G_2}{G_1}$	k	$\frac{G_e}{G_1}$[12]	$\frac{G_e}{G_1}$ (present)
Case 1	$\frac{3}{4}$	$\frac{1}{8}$	$\frac{1}{2}$	30	8	1.2330	1.2924
Case 2	$\frac{3}{4}$	$\frac{1}{8}$	$\frac{1}{2}$	5	3	1.0466	1.0742
Case 3	$\frac{1}{2}$	$\frac{1}{4}$	0	29.4	4	1.5706	1 .7740

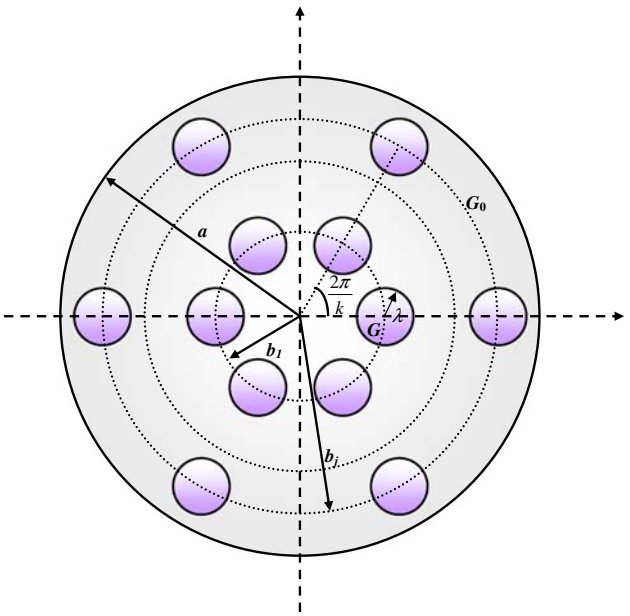

Fig. 9 A *circular rod* with several *rings* of circular inclusions

Table 6 Torsional rigidity of different cases for a circular bar with two and three rings of holes or inclusions

Case	$\frac{b_1}{a}$	$\frac{b_2}{a}$	$\frac{b_3}{a}$	$\frac{\lambda}{a}$	$\frac{G}{G_0}$	j	k	$\frac{G_{eff}}{G_0}$[13]	$\frac{G_{eff}}{G_0}$ (present)
1	$\frac{3}{8}$	$\frac{3}{4}$	–	$\frac{1}{8}$	30	2	6	1.1205	1.3553
2	$\frac{1}{4}$	$\frac{17}{32}$	$\frac{13}{16}$	$\frac{3}{32}$	30	3	6	1.0618	1.2332
3	$\frac{3}{8}$	$\frac{3}{4}$	–	$\frac{1}{8}$	0	2	6	0.9636	0.7493
4	$\frac{1}{4}$	$\frac{17}{32}$	$\frac{13}{16}$	$\frac{3}{32}$	0	3	6	0.9745	0.7800

The geometry sketch is shown in Fig. 9. The results of our approach and those of Kuo and Conway are shown in Table 6. In a similar situation of the previous example, the torsional rigidities deviate with those of Kuo and Conway's result. The reason may be explained in a similar way of Example 3.

Example 5 A *circular rod* with three circular inclusions.

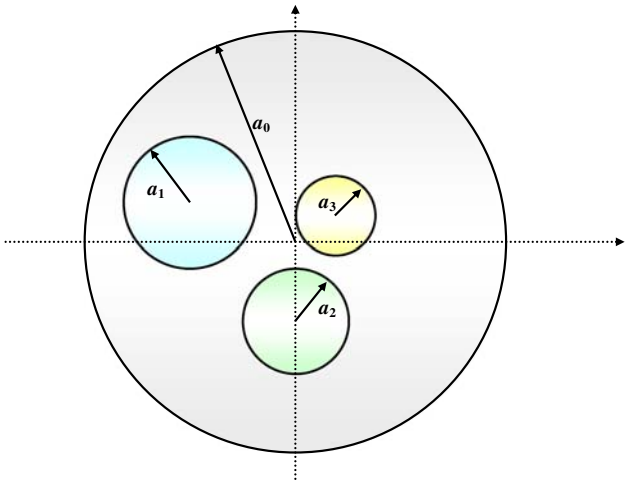

Fig. 10 A *circular bar* with three arbitrary circular inclusions

In this example, we design a circular rod with three arbitrary circular inclusions as shown in Fig. 10. The centers of three inclusions are (−4, 1), (0, 1.732) and (0.75, 0.5). The radii of the circular bar and three inclusions are 0.4, 1.25, 1 and 0.5, respectively. The shear moduli are given as 1.0, 1.5, 2.25 and 0.5. For the case, the torsional rigidity is obtained as 1.11018 by using the present approach. The torsional rigidity of the circular holes is found to be 0.53209 by setting zero moduli of the three inclusions as a special case. The case shows the great generality of the present approach to deal with the problem of a torsion bar with arbitrary number, radii and position inclusions and/or holes.

5 Conclusions

Torsion problems with circular inclusions as well as holes have been successfully solved by using the present formulation. Here, we presented a different way to avoid the singular and hypersingular integrals by kernel separation instead of conventional bump contour approach. Our solutions match well with the exact solution if available and other solutions by using the integral formulation. Only 41 collocation points uniformly distributed on each boundary are required to obtain the accurate results of torsional rigidity with error less than 1% after comparing with the exact solution. For the stress response, our approach also agrees well with the analytical solution. The program was developed to deal with arbitrary number, different positions, various radii and shear moduli of inclusions. The proposed approach is free from calculating principal value, of boundary-layer effect, while the exponential convergence and the meshless method are included in the original elements and advantages of the method. Besides, the BIEs for the domain point or the null-field equation in our formulation can both be employed by exactly collocating the

point on the real boundary thanks to the introduction of the degenerate kernels.

References

1. Ang WT, Kang I (2000) A complex variable boundary element method for elliptic partial differential equations in a multiply-connected region. Int J Comput Math 75:515–525
2. Bird MD, Steele CR (1991) Separated solution procedure for bending of circular plates with circular holes. J Appl Mech 59:398–404
3. Caulk DA (1983) Analysis of elastic torsion in a bar with circular holes by a special boundary integral method. J Appl Mech 50:101–108
4. Chen JT, Chen PY (2007) A semi-analytical approach for stress concentration of cantilever beams with holes under bending. J Mech 23(3):211–221
5. Chen JT, Chiu YP (2002) On the pseudo-differential operators in the dual boundary integral equations using degenerate kernels and circulants. Eng Anal Bound Elem 26:41–53
6. Chen JT, Hong H-K (1999) Review of dual boundary element methods with emphasis on hypersingular integrals and divergent series. Appl Mech Rev 52:17–33
7. Chen JT, Shen WC, Chen PY (2006) Analysis of circular torsion bar with circular holes using null-field approach. CMES 12:109–119
8. Chen T, Weng IS (2001) Torsion of a circular compound bar with imperfect interface. J Appl Mech 68:955–958
9. Crouch SL, Mogilevskaya SG (2003) On the use of Somigliana's formula and Fourier series for elasticity problems with circular boundaries. Int J Numer Methods Eng 58:537–578
10. Jin B (2004) A meshless method for the Laplace and biharmonic equations subjected to noisy boundary data. CMES 6:253–262
11. Katsikadelis JT, Sapountzakis EJ (1985) Torsion of composite bars by boundary element method. J Eng Mech 111:1197–1210
12. Kuo YM, Conway HD (1973) The torsion of composite tubes and cylinders. Int J Solids Struct 9:1553–1565
13. Kuo YM, Conway HD (1974) Torsion of cylinders with multiple reinforcement. J Eng Mech Div 100:221–233
14. Ling CB (1947) Torsion of a circular tube with longitudinal circular holes. Q Appl Math 5:168–181
15. Lurje AI (1970) Theory of elasticity. Nauka Publisher, Moscow (in Russian)
16. Mogilevskaya SG, Crouch SL (2001) A Galerkin boundary integral method for multiple circular elastic inclusions. Int J Numer Methods Eng 52:1069–1106
17. Morse PM, Feshbach H (1978) Methods of theoretical physics. McGraw-Hill, New York
18. Murakami H, Yamakawa J (1998) Torsional wave propagation in reinforced concrete columns. Int J Solids Struct 35:2617–2637
19. Muskhelishvili NI (1963) Some basic problems of the mathematical theory of elasticity. P. Noordhoff, Groningen
20. Naghdi AK (1991) Bending of a perforated circular cylindrical cantilever. Int J Solids Struct 28(6):739–749
21. Petrov EP (1997) Analysis of torsion and shear characteristics of beam cross-sections by the boundary element method. Int J BEM Commun 8:239–245
22. Sapountzakis EJ, Mokos VG (2001) Nonuniform torsion of composite bars by boundary element method. J Eng Mech, ASCE 127(9):945–953
23. Sapountzakis EJ, Mokos VG (2003) Warping shear stresses in nonuniform torsion of composite bars by BEM. Comput Methods Appl Mech Eng 192:4337–4353
24. Sapountzakis EJ, Mokos VG (2004) Nonuniform torsion of composite bars of variable thickness by BEM. Int J Solids Struct 41(7):1753–1771
25. Shams-Ahmadi M, Chou SI (1997) Complex variable boundary element method for torsion of composite shafts. Int J Numer Methods Eng 40:1165–1179
26. Sladek V, Sladek J, Tanaka M (2005) Local integral equations and two meshless polynomial interpolations with application to potential problems in non-homogeneous media. CMES 7:69–84
27. Tang RJ (1996) Torsion theory of the crack cylinder. Shanghai Jiao Tong University Publisher, Shanghai (in Chinese)
28. Timoshenko SP, Goodier JN (1970) Theory of elasticity. McGraw-Hill, New York